Corresponding Author: Mr. Karthik Kashinath,

Corresponding Author's Institution: University of Cambridge

First Author: Karthik Kashinath

Order of Authors: Karthik Kashinath; Santosh Hemchandra, PhD; Matthew P Juniper, PhD

Manuscript Region of Origin:

Nonlinear thermoacoustics of ducted premixed flames: the influence of perturbation convection speed

Karthik Kashinath[a,*], Santosh Hemchandra[b], Matthew P. Juniper[a]

[a]*University of Cambridge, Department of Engineering, Trumpington Street, Cambridge CB2 1PZ*
[b]*Department of Aerospace Engineering, Indian Institute of Science, Bangalore 560012, India*

Abstract

When a premixed flame is placed within a duct, acoustic waves induce velocity perturbations at the flame's base. These travel down the flame, distorting its surface and modulating its heat release. This can induce self-sustained thermoacoustic oscillations. Although the phase speed of these perturbations is often assumed to equal the mean flow speed, experiments conducted in other studies and Direct Numerical Simulation (DNS) conducted in this study show that it varies with the acoustic frequency. In this paper, we examine how these variations affect the nonlinear thermoacoustic behaviour. We model the heat release with a nonlinear kinematic *G*-equation, in which the velocity perturbation is modelled on DNS results. The acoustics are governed by linearised momentum and energy equations. We calculate the flame describing function (FDF) using harmonic forcing at several frequencies and amplitudes. Then we calculate thermoacoustic limit cycles and explain their existence and stability by examining the amplitude-dependence of the gain and phase of the FDF. We find that, when the phase speed equals the mean flow speed, the system has only one stable state. When the phase speed does not equal the mean flow speed, however, the system supports multiple limit cycles because the phase of the FDF changes significantly with oscillation amplitude. This shows that the phase speed of velocity perturbations has a strong influence on the nonlinear thermoacoustic behaviour of ducted premixed flames.

Keywords: nonlinear thermoacoustics, premixed flame, flame describing function, travelling wave, limit cycle amplitude, limit cycle stability

Nomenclature

ϕ Equivalence ratio

$\tilde{u}$ Streamwise velocity

$\tilde{v}$ Transverse velocity

ω Angular frequency

k Wavenumber

*Corresponding author address: ISO40, Department of Engineering, Trumpington Street, Cambridge - CB2 1PZ, U.K., Phone number +44(0)7770661298
  Email address: kk377@cam.ac.uk (Karthik Kashinath)

c Phase speed

K Ratio of steady streamwise base flow velocity to streamwise phase speed, $\tilde{u}_0/c_x$

f_{exc} Forcing frequency

i The complex number $\sqrt{-1}$

ϵ Velocity perturbation amplitude normalized by its steady value

$\Delta\phi$ Velocity perturbation phase

R Slot half-width

L_f Nominal flame height

β_f Flame aspect ratio $= {}^{L_f}/_R$

s_L Laminar flame speed

s_{Lu} Unstretched laminar flame speed

T_u Unburned gas temperature

p Pressure

ρ Density

γ Ratio of specific heats

Y Mass fraction

W Molecular weight

L_u Markstein length

St Strouhal number $= 2\pi f_{exc}\beta_f R/\tilde{u}_0$

G Level Set (function of space and time), $G=0$ represents the flame surface

A Instantaneous flame surface area

s_L Laminar flame speed

h_R Heat of reaction (per unit mass)

$\dot{Q}$ Heat release rate

$\tilde{c}_0$ Speed of sound

M Mach Number

$\delta()$ Dirac delta function

L_0 Length of duct

2

x_f Flame position in the duct normalised by length of duct

ζ Damping parameter

c_1 Damping factor corresponding to acoustic radiation

c_2 Damping factor corresponding to boundary layer losses

ω_1 Fundamental acoustic frequency of the duct

ν Viscosity

χ Thermal conductivity

E Acoustic energy density

T Acoustic time period of one cycle of oscillation at the fundamental frequency

φ Phase of any quantity in a Fourier expansion

f^* Non-dimensional fundamental frequency of the self-excited system, $f^* = \tilde{c}_0 L_f / 2 u_0 L_0$

Modifiers

$(\hat{\cdot})$ Fourier component at the forcing St

$(\cdot)_x$ Streamwise quantity

$(\cdot)_y$ Transverse quantity

$(\cdot)'$ Perturbation about the steady value

$(\cdot)_0$ Steady base flow value

$|\cdot|$ Magnitude of perturbations or gain of a function

$\angle \cdot$ Phase of perturbations or a function

$\tilde{(\cdot)}$ Dimensional quantity

$(\cdot)^*$ Non-dimensional quantity

$\langle \cdot \rangle$ Time average of the quantity over a forcing cycle

1. Introduction

Models of thermoacoustic systems contain a model for the heat release rate and a model for the acoustics. This paper concerns the model for the heat release rate of premixed flames. One approach is to model the flame surface as a zero-contour of a continuous function G. The flame propagates normal to itself, while also being advected by the surrounding flow. This is known as the G-equation model and is often used in models of thermoacoustic systems, either directly [1–3] or in the form a kinematic flame-tracking equation derived from the G-equation model [4–8]. In this model, the velocity field influences the heat release rate by distorting the flame's surface.

The velocity field can be decomposed into a steady base flow and acoustic, vortical and entropy perturbations [9]. Acoustic waves induce velocity perturbations at the base of the flame by exciting a convectively unstable shear layer. These velocity perturbations then travel along the flame, distorting its surface and therefore causing flame area fluctuations that result in unsteady heat release rate oscillations.

Several studies have investigated in detail the receptivity of shear layers to acoustic forcing and the enhanced generation of vorticity in separated shear layers by acoustic forcing, but most of these studies were for non-reacting flows. These have been reviewed by Wu *et al.* [10]. Similar studies for reacting shear layers are fewer, but are receiving more attention in recent years [11–13]. While these studies have generated a wealth of information about the response of shear layers to acoustic forcing, measurements or calculations of the phase speed of shear layer disturbances are limited, especially in the reacting case.

Experiments on laminar premixed flames by Boyer and Quinard [14] show that the hydrodynamic feedback from the flame changes the flow upstream, makes the acoustic field non-uniform and in particular, alters the convective speed of vortices that distort the flame surface. Experiments on forced conical premixed flames by Baillot *et al.* show that the disturbance propagation speed depends on the frequency but is independent of spatial location [15]. Velocity field measurements of an oscillating bunsen flame by Ferguson *et al.* show that streamwise disturbances are transported at a speed different from the average flow velocity [16]. Birbaud *et al.* investigated flows in acoustically excited free jets and premixed conical flames and found different oscillatory regimes that depend on the forcing frequency [17, 18]. In the convective regime they found that the perturbation convection speed depends on the forcing frequency and the distance from the burner exit plane but is independent of the forcing amplitude [17]. This is the most detailed study of the upstream flow dynamics of an acoustically forced bunsen flame. Durox *et al.* in their study of the acoustic response of various configurations of laminar premixed flames point out that an accurate description of the oscillating flow field, including the fluid motion in the shear layer region, is crucial to capture the flame response [19, 20]. Kornilov *et al.* show using particle image velocimetry measurements in a multi-slit burner that travelling waves are generated just upstream of the burner exit plane due to acoustic forcing [21, 22]. Karimi *et al.* show clearly from measurements of the perturbed flame surface of a forced bunsen flame that the disturbance convection speed along the flame is not equal to the mean flow [23]. They use their measured perturbation convection speeds to make more accurate estimates of the phase of the flame describing function.

Experiments on a slot burner by Kartheekeyan and Chakravarthy and experiments on rod-stabilized flames and bluff-body stabilized flames by Shanbhogue *et al.* and Shin *et al.* show that the vortices that roll up in the acoustically excited shear layer convect along the flame at a speed not necessarily equal to the mean flow and usually slightly lower than the mean flow [24–26, 6]. O'Connor *et al.* study the

hydrodynamics of transversely excited swirling flow fields, both non-reacting and reacting, and show that the amplification of acoustic disturbances by convectively unstable shear layers dominate the wrinkling and dynamics of the flame [27–29]. Due to the multi-dimensional disturbances in their configuration, however, it was too complicated to extract a single phase speed of perturbations.

It is clear from the above studies that the disturbance characteristics in acoustically excited shear layers have a significant impact on the flame response and in particular, the convection speed of perturbations depends on several parameters and is not equal to the mean flow velocity.

These velocity perturbations that distort the flame surface are usually assumed to take the form of a traveling wave $\exp\left[i(kx - \omega t)\right]$, for which the streamwise phase speed, c_x, is equal to ω/k. The ratio of the mean velocity, u_0, to this phase speed, c_x, is denoted K. Most models assume that the phase speed is equal to the mean flow velocity, *i.e.* that $K = 1$ [30–32]. Preetham *et al.* investigate the influence of the parameter K on the gain and phase of the transfer function and they conclude that nonlinear effects are enhanced for $K > 1$ [1]. They, however, do not measure the dependence of K on frequency and amplitude of the acoustic perturbations in their analysis.

Our previous work on a simple thermoacoustic system containing a G-equation model of a premixed flame showed that, if $K = 1$, the system has at most one limit cycle and that this limit cycle must be stable [33]. However, recent experiments on similar systems show that there can be several limit cycles and that some are unstable [34–36]. Our analysis [33] captured this behaviour when K was greater than 1, but we did not justify this. In this paper we justify the values of K for the simple thermoacoustic system of a ducted premixed flame. The aims of this paper are (i) to extract K from Direct Numerical Simulation (DNS) of a premixed flame in order to provide an improved velocity perturbation model for inclusion in the G-equation; (ii) to use the G-equation model to calculate the flame describing function (FDF) between acoustic forcing and heat release response; (iii) to calculate the nonlinear behavior of the coupled self-excited thermoacoustic system and to explain its origin using the FDF.

2. DNS of a laminar premixed flame

The configuration studied consists of a 2-D slot-stabilized premixed methane-air flame inside a tube (Fig. 1). DNS of the fully compressible Navier–Stokes equations for reacting flows are performed using
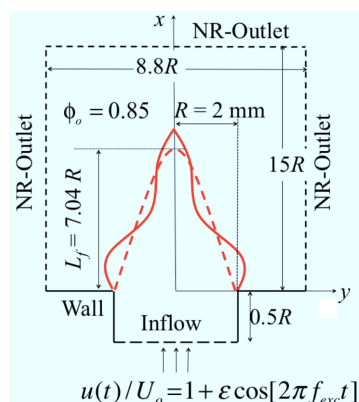

Figure 1: Schematic of the 2-D slot-stabilized premixed methane air flame. The dashed line represents the steady flame contour and the solid curve represents an instantaneous forced flame contour. NR stands for non-reflecting boundary conditions.

explicit eighth order central differences for spatial derivatives and a third order Runge-Kutta scheme for time integration. Tenth order spatial filtering is performed after every two timesteps to remove spurious numerical oscillations [37]. This DNS code has been recently used for premixed flames subjected to fuel-air ratio fluctuations [38]. The kinetic scheme is a single step irreversible global reaction used by Lacaze *et al.* [39] as follows. Chemical source terms are determined assuming a single step and irreversible global reaction: $CH_4 + 2O_2 \longrightarrow CO_2 + 2H_2O$. The reaction rate, $\dot{\omega}$, is determined from the mass fractions of methane, Y_{CH_4} and oxygen, Y_{O_2}, using the following expression (Lacaze *et al.* [39]):

$$\dot{\omega} = A\Big(\frac{\rho Y_{CH_4}}{W_{CH_4}}\Big)\Big(\frac{\rho Y_{O_2}}{W_{O_2}}\Big) \exp\Big(-\frac{E_a}{R_u T}\Big) \tag{1}$$

where, $A = 6.9 \times 10^{14}$ cm^{-3} mol^{-1} s^{-1}, $E_a = 132.1642$ kJ mol^{-1} and R_u is the universal gas constant. Figure 2 shows the variation of the unstretched laminar flame speed, s_{Lu}, as a function of ϕ computed using
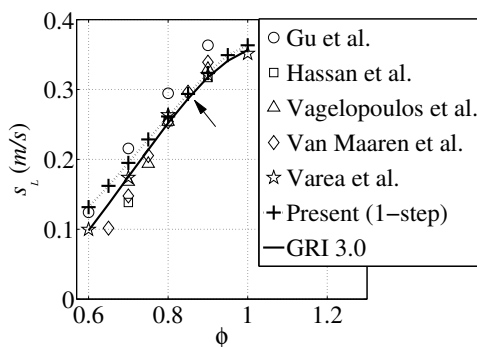

Figure 2: Variation of the laminar flame speed with the equivalence ratio (ϕ) for Methane-air flames. ($T_u = 300$ K, $p_o = 1$atm). The arrow shows the point corresponding to $\phi_o = 0.85$ at which forced computations are performed in this study. Figure reprinted from [38].

the above mechanism (see [38] for details).

The temperature-dependent thermodynamic properties, the viscosity, and the thermal conductivity for all species are determined from theoretically-derived functions of temperature [40]. Mixture viscosity and thermal conductivity are determined from corresponding values for pure species using averaging rules [41, 42]. Mixture diffusivities of individual species are determined from their corresponding Lewis numbers (assumed constant).[1]

The domain is discretized using a structured mesh with nominal grid spacing of 40 μm. The reaction zone of the flame is always resolved over 10-15 grid points in these simulations. Grid independence has been checked by computing steady flames on successively refined grids up to a nominal grid size of 20 μm. The maximum change in computed solutions (across all flow variables and grid points) due to grid refinement, relative to the values on the nominal grid, is 8%.

A top-hat mean inlet velocity profile ($\tilde{u}_0 = 2.52$ ms^{-1}) is specified with an inlet boundary layer thickness of $0.2R$ and a constant temperature of 300 K. The wall temperature smoothly increases from 300 K at the inlet duct to 1200 K along the dump plane, across the 1 mm vertical section. The 2.4 mm horizontal section

---

[1]Lewis Numbers: CH$_4$ = 0.97, O$_2$ = 1.11, CO$_2$ = 1.39, H$_2$O = 0.83.

(labelled "wall" in Fig. 1) is at a constant temperature of 1200 K. This ensures that the flame remains attached to the slot lip. An isothermal boundary condition was found to cause the flame to lift off. The wall temperature distribution was maintained constant at all times during the simulations.

We have chosen to anchor the base of the flame to a particular point in this study, in order to study only the influence of the perturbation convection speed. Motion of the flame base can have a significant influence on the overall system behaviour (see for example [21, 1, 43]). Experiments on forced premixed flames, however, show that flame base motion significantly affects the nonlinear flame response only at large forcing amplitudes [23]. We have also chosen to ignore flame lift-off. Recent experiments on a self-excited ducted premixed flame show that flame lift-off occurs at large velocity fluctuation amplitudes and can lead to complicated nonlinear behaviour such as intermittency, ultimately leading to flame blow-out [36, 44]. These results imply that our attached flame assumption will not be accurate for very large amplitude velocity fluctuations, however, they will be valid when the flame remains attached to the burner lip or when lift-off is prevented, for example by using a pilot flame.

These conditions yield a nominally steady flame with $\beta_f = L_f/R = 7.0$ (see Fig. 1). The inlet flow velocity is forced harmonically, $u(t)/\tilde{u}_0 = 1 + \varepsilon \cos[2\pi f_{exc}t]$, where the forcing frequency, f_{exc}, varies between 80 Hz and 460 Hz, and the forcing amplitudes, ε, are 0.05, 0.1 and 0.2. The global heat release response is found by integrating the volumetric heat release rate over the domain, 20 times per forcing cycle. The non-dimensional forcing frequency is represented by the Strouhal number, St (St$=f_{exc}L_f/\tilde{u}_0$) and varies between 0.44 (80 Hz) and 2.56 (460 Hz). The measured velocity fields are used to construct a reduced order velocity model, as described next.

2.1. Reduced order model for the velocity field

The perturbation velocity field, $u'(x, y, \varepsilon, \omega)$, is assumed to be of the form $\varepsilon \exp(\mathrm{i}(k_x x + k_y y - \omega t))$. The local wavenumbers in the x and y directions, k_x and k_y, depend on the frequency and amplitude of the forcing, and on the spatial location. By differentiating u' with respect to x and then to y the following relationships for the local wavenumbers are obtained:

$$\mathrm{i}k_x = \frac{1}{u'}\frac{\partial u'}{\partial x}; \quad \mathrm{i}k_y = \frac{1}{u'}\frac{\partial u'}{\partial y}. \tag{2}$$

The phase speeds in the x and y directions, c_x and c_y, are related to the forcing frequency, ω, and real components of k_x and k_y by $c_x = \omega/k_{x,r}$ and $c_y = \omega/k_{y,r}$.

Figures 3 (a) and (b) show the streamwise variation of the normalized velocity perturbation phase relative to the inlet, $\Delta\phi\beta_f/$St ($\Delta\phi = \angle\hat{u}' - \angle\hat{u}'_{inlet}$), at different transverse locations. The streamwise variation is shown up to the flame position at each transverse location, *i.e.* at points that are always upstream of the flame. The slopes of these curves give the non-dimensional phase speeds upstream of the flame. The slope for an acoustic wave is shown by the dot-dashed line (slope$=-$M$=-\tilde{u}_0/\tilde{c}_0$) and that for a convective wave with phase speed equal to the mean flow speed ($K = 1$) is shown by a thin solid line (slope$=-1$).

Firstly, the phase is almost independent of the transverse coordinate, showing that the transverse wavenumber, k_y, is very small and the transverse phase speed, c_y, is very large, as seen in experiments by Birbaud *et al.* [17]. Secondly, the slope is uniform in the streamwise direction, except around the base and tip of the flame, showing that the streamwise wavenumber, k_x, and streamwise phase speed, c_x are
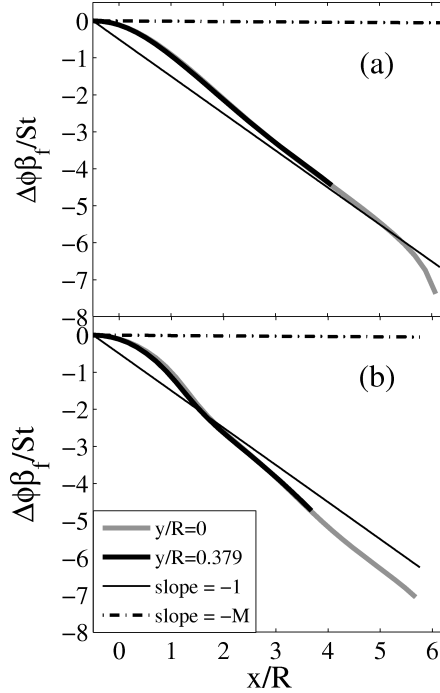
Figure 3: Variation of normalized velocity perturbation phase, $\Delta\phi\beta_f/$St, along the streamwise coordinate, x/R, at different transverse coordinates, y/R, at $\phi = 0.85$ and $\varepsilon = 0.05$ for (a) $f_{exc} = 160Hz$ (St $= 0.88$) and (b) $f_{exc} = 320Hz$ (St $= 1.76$). The slope of the streamwise variation of the normalized phase is the non-dimensional phase speed of the velocity perturbations in the flow upstream of the flame. The normalized slope for an acoustic wave is shown by the dot-dashed line and for a convective wave with phase speed equal to the mean flow speed is shown by the thin solid black line.

mostly uniform. Close to the base, the slope is approximately $-$M because the acoustic perturbation components dominate in this inlet region and the wavelength is much larger than the flame length, as seen in experiments with conical flames by Birbaud *et al.* [17]. Most significantly, the overall slope is not exactly equal to -1, which means that the phase speed is not equal to the mean flow speed. This has important consequences for the nonlinear dynamics of these flames [1, 33].

Figures 4 (a) and (b) show the normalized velocity perturbation phase, $\Delta\phi\beta_f/$St ($\Delta\phi = \angle\hat{u}' - \angle\hat{u}'_{inlet}$), along the centreline, $y/R = 0$, at three forcing amplitudes. The lines overlap, showing that the phase speed (and therefore the local wavenumber) is independent of the forcing amplitude, as noticed in experiments [17]. For the range of amplitudes examined in this study the phase speed was found to be independent of the amplitude, but we expect that this will not be true at very large forcing amplitudes. This shows that the perturbation travels in the streamwise direction with a nearly constant phase speed, which depends only on the forcing frequency. This allows us to simplify the model for u' to be of the form $\varepsilon \exp i(k_x x - \omega t)$, where k_x is a function of the forcing frequency alone. This can be written: $k_x = \omega/c_x = (\omega/u_0) * K$.

Figure 5 shows K as a function of the forcing frequency, St, for six forced DNS runs. The solid line is a least squares quadratic fit to these data, which is used for the G-equation model in this paper. Although K is often assumed to equal 1 for G-equation models used in thermoacoustic systems [30–32], experiments have shown that this is not necessarily true [14, 15, 19, 17, 24, 25, 20, 23, 26–28, 6]. Figure 5 shows that this is not the case for the flame examined in this study. This figure shows that, for this particular flame, the perturbation phase speed is always lower than the mean flow velocity, except at St ≈ 1.5, when
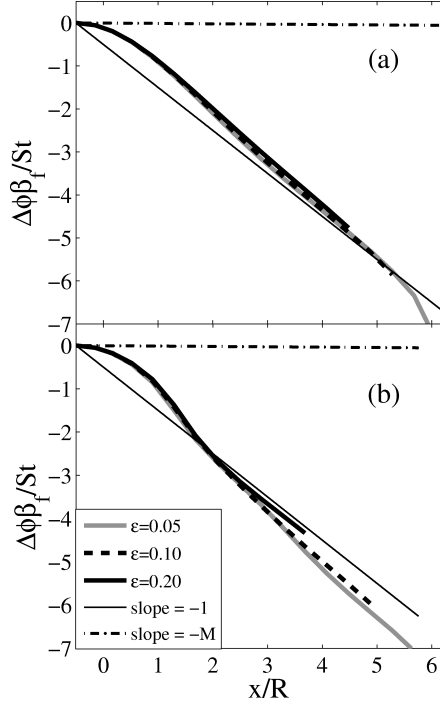
Figure 4: Variation of normalized velocity perturbation phase, $\Delta\phi\beta_f$/St, along the centreline, $y/R = 0$, at different forcing amplitudes, $\varepsilon = 0.05, 0.10, 0.20$ for (a) $f_{exc} = 160Hz$ and (b) $f_{exc} = 320Hz$. The overlap of the plots shows clearly that the phase speed is independent of the forcing amplitude.

the perturbation phase speed is equal to the mean flow velocity. These values of K, however, cannot be generalised without performing detailed analysis into the hydrodynamic response of the flow field for different flame and flow configurations using either experiments or DNS.
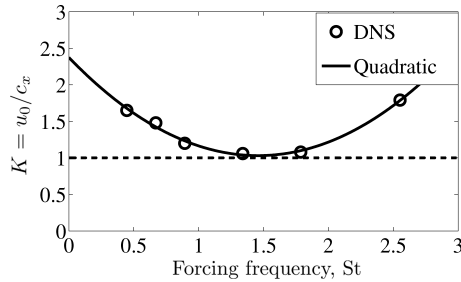

Figure 5: Ratio of the mean velocity to the disturbance phase speed, $K = u_0/c_x$, as a function of the forcing frequency, St, for $\phi = 0.85$. The solid line is a quadratic fit to the DNS data, which are shown as circles. The equation of the fit is $K = 0.631\text{St}^2 - 1.841\text{St} + 2.374$. Most models assume that $K = 1$ [30–32], shown by the horizontal dashed line.

The transverse perturbation velocity upstream of the flame, v', is determined using the incompressible continuity equation with $v' = 0$ at $y = 0$ [31]:

$$\frac{\partial u'}{\partial x} + \frac{\partial v'}{\partial y} = 0; \quad \frac{\partial \hat{v'}}{\partial y} = -ik_x\hat{u'}; \quad \hat{v'} = -ik_x\hat{u'}y. \tag{3}$$

Figure 6 shows the ratio of the transverse velocity perturbation, v', to the streamwise velocity perturbation,

9

u', across the transverse coordinate, y/R. Points of v'/u' are plotted only for values where the temperature rise is less than 5% of the total temperature rise. These points are extracted from the forced DNS data at (a) St = 0.44 and (b) St = 1.78. The ratio of v'/u' is almost linear, except very close to the flame because of the sharp density gradient due to the temperature rise. This shows that the incompressible continuity equation (3) provides a very good approximation to v' upstream of the flame, which is the relevant region to consider for velocity perturbations in the G-equation model. In subsequent sections, this velocity model is combined with the G-equation model and used for a range of linear and nonlinear simulations of the forced flame response, in order to extract the FDF.
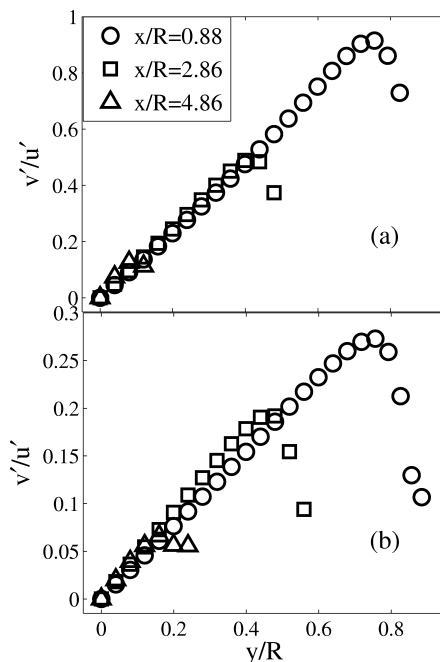

Figure 6: Ratio of transverse velocity to streamwise velocity perturbation, v'/u', across the transverse coordinate, y/R, derived from DNS at $\phi = 0.85$ and $\varepsilon = 0.05$ for (a) St = 0.44 and (b) St = 1.78. The transverse variation is shown up to the flame position at each streamwise location. In the unreacted stream, v'/u' is a linear function of y, in accordance with Eq. (3).

3. Reduced order model of the premixed flame: The G-equation

The flame is described by a kinematic model based on the level set method proposed by Williams [45], which is also known as the G-equation model. This model has been shown to capture the major nonlinearities in premixed flame dynamics [4, 46] and has been used widely in low-order models of thermoacoustic systems with premixed flames [4, 7, 8, 31].

The principal assumptions of the model are that (1) the flame is a thin surface separating unburnt reactants from burnt products; (2) the influence of gas expansion across the flame front is negligible [43]. Assumption (1) allows for the flame to be tracked using the G-equation, which for the present two-dimensional

case can be written as [45]:

$$\frac{\partial G}{\partial \tilde{t}} + \tilde{u}\frac{\partial G}{\partial \tilde{x}} + \tilde{v}\frac{\partial G}{\partial \tilde{y}} = s_L\sqrt{\left(\frac{\partial G}{\partial \tilde{x}}\right)^2 + \left(\frac{\partial G}{\partial \tilde{y}}\right)^2} \tag{4}$$

where $G(\tilde{x}, \tilde{y}, \tilde{t})$ is a time-varying function that is negative in the unburnt gas, positive in the burnt gas and zero on the flame surface. The flow is perfectly premixed and flame stretch effects are neglected, hence the flame speed is uniform. The flame speed $s_L(\phi)$ for the G-equation computations is determined from a curve fit to the data from the 1-step computations in fig. 2 as follows,

$$s_L(\phi) = 0.42\phi^{-1.0306}\exp[-5.2801(\phi - 1.1644)^2] \tag{5}$$

For all cases analysed in this paper, $\phi = 0.85$ and $s_L = 0.295\ m/s$. Equation (4) can be rewritten in terms of non-dimensional parameters: $x^* = \tilde{x}/L_f, y^* = \tilde{y}/R, u = \tilde{u}/\tilde{u}_0, v = \tilde{v}/\tilde{u}_0, t^* = \tilde{t}\tilde{u}_0/L_f$ as

$$\frac{\partial G}{\partial t^*} + u\frac{\partial G}{\partial x^*} + \beta_f v\frac{\partial G}{\partial y^*} = \left(\frac{s_L}{\tilde{u}_0}\right)\sqrt{\left(\frac{\partial G}{\partial x^*}\right)^2 + \beta_f^2\left(\frac{\partial G}{\partial y^*}\right)^2} \tag{6}$$

Assumption (2) allows for the velocity field to be independently specified, neglecting the coupling between the flow-field and flame surface evolution, and is the major simplifying assumption of this approach. In §2.1 we showed that the non-dimensional streamwise velocity field can be specified as a harmonically oscillating travelling wave, with the transverse velocity obtained by solving the incompressible continuity equation:

$$u = u(t)/\tilde{u}_0 = 1 + \varepsilon\cos(2\pi\mathrm{St}(Kx^* - t^*)), \tag{7}$$

$$v = v(t)/\tilde{u}_0 = \frac{2\pi\varepsilon\mathrm{St}Ky^*}{\beta_f}\sin(2\pi\mathrm{St}(Kx^* - t^*)), \tag{8}$$

where K is obtained from the quadratic fit in Fig. 5.

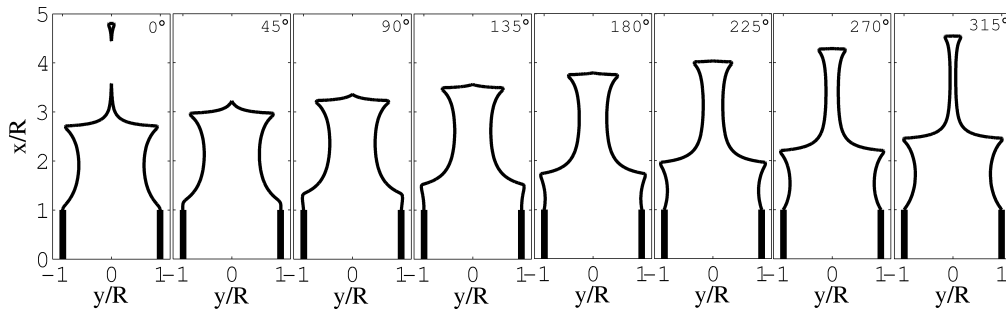Equation (4), with the velocity field specified as above, is solved numerically using a 5th order Weighted

Figure 7: Instantaneous images of the flame during one forcing cycle, $\phi = 0.85$, $\beta_f = 5$, $\varepsilon = 0.4$, St $= 2$, $K = 1.18$. Note the formation of sharp cusps towards the products and flame pinch-off, which are distinct characteristics of premixed flames seen in several experiments [14, 15, 5, 19, 17, 23]

Essentially Non-Oscillatory (WENO) scheme [47] and a 3rd order Total Variation Diminishing (TVD) Runge-Kutta scheme [48] for time integration. The non-dimensionalized spatial and temporal resolution in all the simulations are 5×10^{-3} and 5×10^{-4} respectively, with a uniform mesh spacing in both spatial directions.

The local level set method is used to achieve a significant reduction in computational cost [49]. The boundary condition on the centerline (y=0) is symmetry, so we solve the G-equation only for one half of the flame. The boundary conditions on the other boundaries of the domain (top, bottom and right) are not needed because we use a local level-set method and the flame never reaches these boundaries for the range of conditions examined in this paper. The flame base is assumed to be anchored at a fixed location by specifying zero velocity in this region (hence the G-field does not advect here). These computations are performed within the framework of LSGEN2D, a general level set method solver, developed by Hemchandra [43]. Figure 7 shows instantaneous flame images over one forcing cycle. The cusp formation and flame pinch-off found here have also been observed in several experiments [14, 15, 5, 19, 17, 23].

For a premixed flame, the heat release rate is evaluated using an integral over the whole domain,

$$q(t) = \int_D \rho s_L h_R \left| \nabla G \right| \delta(G) dx^* dy^*. \tag{9}$$

This equation is evaluated numerically using the method described by Smereka [50].

4. Governing equations for the acoustics

For simplicity, the acoustic chamber in the thermoacoustic system considered here is a duct open at both ends as shown schematically in Fig. 8.
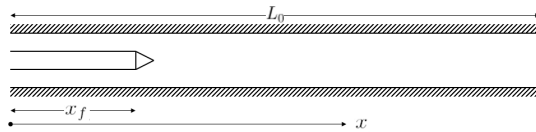

Figure 8: Schematic of the flame in a duct.

The base flow velocity, pressure, density and speed of sound are assumed to be uniform. The Mach number, $M \equiv \tilde{u}_0/\tilde{c}_0$, is assumed to be small, implying that nonlinear acoustic effects can be neglected. This is a reasonable assumption for gas turbine combustors, in which the normalized pressure fluctuations are small compared to the normalized velocity fluctuations [51]. A compact flame assumption is used because the flame length is small compared to the acoustic wavelengths. The duct width is 50 times that of the slot width, so the influence of gas expansion on the steady base flow upstream of the flame is assumed to be small [52]. Therefore, the unducted computations using DNS are valid in this configuration. The dimensional governing equations for the acoustic perturbations are the momentum and energy equations:

$$\tilde{\rho}_0 \frac{\partial \tilde{u}}{\partial \tilde{t}} + \frac{\partial \tilde{p}}{\partial \tilde{x}} = 0 \tag{10}$$

$$\frac{\partial \tilde{p}}{\partial \tilde{t}} + \gamma \tilde{p}_0 \frac{\partial \tilde{u}}{\partial \tilde{x}} + \zeta \frac{\tilde{c}_0}{L_0} \tilde{p} - (\gamma - 1)\tilde{\dot{Q}}\delta(\tilde{x} - \tilde{x}_f) = 0 \tag{11}$$

where the rate of heat transfer from the flame to the gas is given by $\tilde{\dot{Q}}$, which is applied at the flame's position, $\tilde{x}_f$. For the open duct examined here, the pressure perturbations and the gradient of the velocity

perturbations are both set to zero at the ends of the tube.

$$[\tilde{p}]_{\tilde{x}=0} = [\tilde{p}]_{\tilde{x}=L_0} = 0; \quad \left[\frac{\partial \tilde{u}}{\partial \tilde{x}}\right]_{\tilde{x}=0} = \left[\frac{\partial \tilde{u}}{\partial \tilde{x}}\right]_{\tilde{x}=L_0} = 0. \tag{12}$$

The acoustic damping, represented by ζ, is the sum of two damping parameters, c_1 and c_2:

$$\zeta = c_1 + c_2 = \frac{R^2 \omega_1^2}{\tilde{c}_0^2} + \frac{\sqrt{2\omega_1} L_0}{\tilde{R}\tilde{c}_0}\left(\sqrt{\tilde{\nu}} + \sqrt{\tilde{\chi}}(\gamma - 1)\right). \tag{13}$$

where c_1 represents acoustic energy losses due to radiation from the open ends and c_2 represents dissipation in the acoustic viscous and thermal boundary layers at the duct walls. This model is based on correlations developed by Matveev [53] and has been used in similar thermoacoustic systems [7, 54]. Typical values for laboratory-scale Rijke tubes are $c_1 \approx 0.01 - 0.13$ and $c_2 \approx 0.005 - 0.03$. In particular, for a Rijke tube of length 70 cm and diameter 10 cm with an average duct temperature of 350K, $c_1 = 0.05$, $c_2 = 0.015$ and $\zeta = 0.065$. Higher values of ζ correspond to shorter, wider tubes and lower values of ζ correspond to longer, thinner tubes.

5. Linear and nonlinear flame response: FDF

Figure 9 shows the gain and phase of the FDF of the heat release rate response to velocity perturbations for K obtained from the DNS (a and b) and for $K = 1$ (c and d). The FDFs were calculated by harmonically forcing the kinematic model of the premixed flame (using the G-equation) and extracting the heat release rate at the forcing frequency, discarding higher harmonics. The forcing frequency, St, was varied from 0.04 to 2.5 in steps of 0.02. The forcing amplitude, ε, was varied from 0.02 to 0.6 in steps of 0.02. The amplitude of the streamwise velocity perturbation, ε, was used to define the FDF.

Figure 9(a) shows that at low forcing amplitudes, the gain exceeds 1 between St=1 and St=2 but drops quickly at higher St. As the forcing amplitude increases, the gain decreases monotonically everywhere, except at the highest St. Figure 9(b) shows that at low forcing amplitudes, the phase depends nearly linearly on St, which is characteristic of systems with a constant time delay. As the forcing amplitude increases, however, the phase changes significantly at a given St. At high St, where the change is particularly large, it is due to the reduction in the mean flame height and the movement of the location of peak heat release closer to the flame base. This has been seen in flame kinematic simulations [1], as well as in experiments [55, 23]. This differs from that of a model with $K = 1$ (Figure 9(d)) in which the FDF phase shows negligible dependence on the forcing amplitude (see Fig. 9(d)), also shown in previous studies [1, 46]. The amplitude-dependence of the phase of the FDF, however, has been shown to be highly influential on limit cycle behaviour [20, 33, 34].

A quantitative comparison of FDFs from the G-equation and DNS is not possible because it is computationally too expensive and would deviate from the focus of this study. The qualitative behaviour of the FTF (flame transfer function, i.e. FDF at at the lowest forcing amplitude) resembles that measured by Kornilov in his PhD thesis (see Fig. 10 reprinted from [56]) but a quantitative comparison is not possible because the mean flow velocity in our numerical simulations (2.52 m/s) is much greater than in Kornilov's experiment (max 1.2 m/s), and as can be seen in Fig. 10, the mean flow velocity has a significant effect on the FTF. A unique feature of the FTF of the 2-D slot-stabilized flame in this study is the initial decrease in gain at
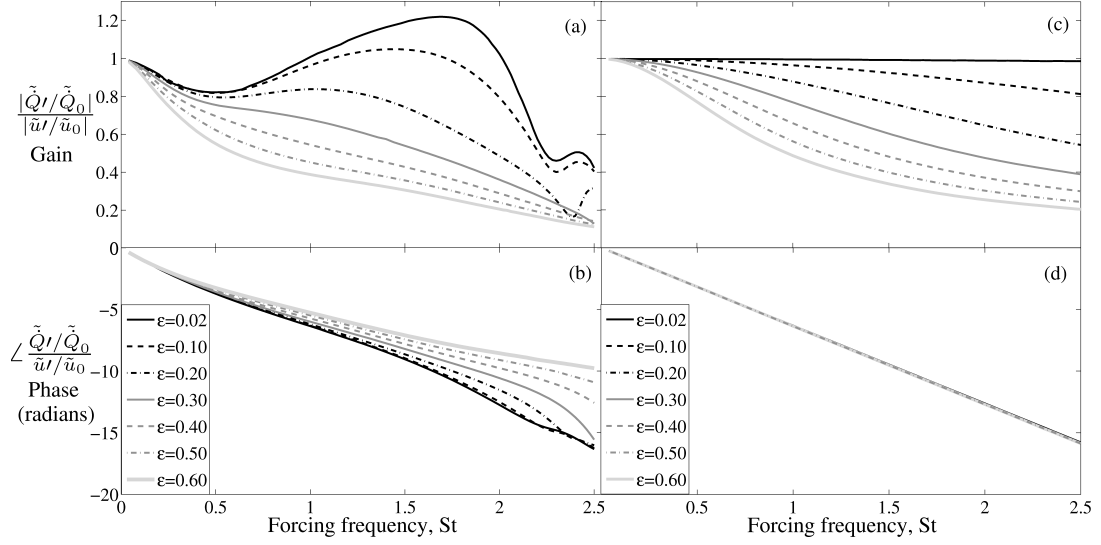
Figure 9: Flame Describing Function, $FDF(\omega,\varepsilon) = \frac{\tilde{Q}'/\tilde{Q}_0}{\tilde{u}'/\tilde{u}_0}$ a) Gain (K from DNS) and b) Phase (K from DNS). Note that as the forcing amplitude increases, the gain decreases monotonically and the phase changes significantly at high St. c) Gain (K = 1) and d) Phase (K = 1). Note that as the forcing amplitude increases, the gain decreases monotonically but the phase has negligible change. $\beta_f = 7$, $\phi = 0.85$
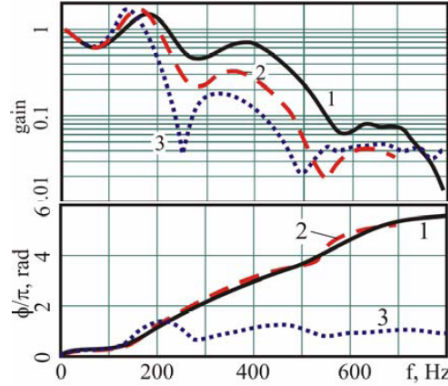

Figure 10: Figure reprinted with permission from V. N. Kornilov, "Experimental research of acoustically perturbed bunsen flames," PhD Thesis, Eindhoven University of Technology (2006) [56]. Copyright ©Eindhoven University of Technology. The Flame Transfer Function, $FTF(\omega) = \frac{\tilde{Q}'/\tilde{Q}_0}{\tilde{u}'/\tilde{u}_0}$ of a multi-slit burner flame, $\phi = 0.9$, 1 - $\tilde{u}_0 = 1.2m/s$, 2 - $\tilde{u}_0 = 1.0m/s$, 3 - $\tilde{u}_0 = 0.8m/s$. The x axis scaling between Fig. 9 and the current figure is St = 1 is approximately $f_{exc} = 180Hz$. The phase plots have opposite signs because of the convention used in defining the phase (lag vs. lead). Note that at low frequencies, the gain decreases as the frequency increases, but rises to values above unity at intermediate frequencies before decreasing at high frequencies, as seen in Fig. 9. The phase is almost linear with frequency, except for the case with lowest mean flow velocity.

low St followed by an increase, with the gain exceeding unity for a range of St, and this compares well with experiments [56].

In §6, we show that the amplitude-dependence of the gain and the phase seen in Fig. 9(a) and (b) greatly affects the limit cycle behaviour of the coupled thermoacoustic system.

6. Nonlinear dynamics and limit cycle behaviour

The method used here is similar to the method of averaging developed by Culick [57]. Culick derived coupled nonlinear first order differential equations for the amplitudes and phases of the acoustic modes which are then solved numerically. Our analysis is simplified by considering only the fundamental acoustic mode. This is a common simplification because (i) higher modes are more heavily damped and (ii) higher harmonics of the heat release are small [34]. However, we extend our analysis to calculate, analytically, limit cycle amplitudes and their stability.

The acoustic velocity perturbation can be written as

$$\tilde{u} = \varepsilon \tilde{u}_0 \cos(\omega \tilde{t}) \cos\left(\frac{\pi \tilde{x}}{L_0}\right). \tag{14}$$

Solving for the acoustic pressure perturbation using Eq. (10) yields

$$\tilde{p} = \varepsilon \tilde{u}_0 \tilde{\rho}_0 \frac{\omega L_0}{\pi} \sin(\omega \tilde{t}) \sin\left(\frac{\pi \tilde{x}}{L_0}\right). \tag{15}$$

The acoustic energy density is written as the sum of potential and kinetic energies,

$$\tilde{E} \equiv \frac{1}{2}\left(\frac{\tilde{p}^2}{\tilde{\rho}_0 \tilde{c}_0^2} + \tilde{\rho}_0 \tilde{u}^2\right). \tag{16}$$

For a thermoacoustic system on a limit cycle, the change in the total acoustic energy in the domain over a cycle of oscillation is zero,

$$\int_{t'}^{t'+T} \int_D \frac{\partial \tilde{E}}{\partial \tilde{t}} \mathrm{d}\tilde{x}\mathrm{d}\tilde{t} = \int_{t'}^{t'+T} \int_D \left(\frac{\tilde{p}}{\tilde{\rho}_0 \tilde{c}_0^2}\frac{\partial \tilde{p}}{\partial \tilde{t}} + \tilde{\rho}_0 \tilde{u}\frac{\partial \tilde{u}}{\partial \tilde{t}}\right)\mathrm{d}\tilde{x}\mathrm{d}\tilde{t} = 0. \tag{17}$$

Using Eqs. (11), (14) and (15), and integrating over the domain $\tilde{x} = [0, L_0]$ yields,

$$\int_{t'}^{t'+T} \left(2\xi \dot{Q}\sin(\omega \tilde{t}) - \frac{\omega L_0}{\pi \tilde{c}_0}\zeta\varepsilon \sin^2(\omega \tilde{t})\right)\mathrm{d}\tilde{t} = 0, \tag{18}$$

$$\xi \equiv \frac{(\gamma - 1)\tilde{Q}_0 \alpha}{\gamma \tilde{p}_0 \tilde{u}_0}\sin\left(\frac{\pi \tilde{x}_f}{L_0}\right), \quad \dot{Q} \equiv \frac{\dot{\tilde{Q}}}{\dot{\tilde{Q}}_0} \tag{19}$$

where $\xi\dot{Q}$ is the nondimensional heat release rate perturbation averaged over the cross-section of the duct.

In general, the heat release rate perturbation in Eq. (18) is nonlinear and can be written as a Fourier series,

$$\dot{Q} = \sum_{j=1}^{\infty} q_j \cos(j\omega \tilde{t} - \varphi_j) \tag{20}$$

Using the orthogonality property, Eq. (18) reduces to

$$\int_{t'}^{t'+T}\left(2\xi q_1 \sin(\varphi_1) - \frac{\omega L_0}{\pi \tilde{c}_0}\zeta\varepsilon\right)\sin^2(\omega \tilde{t})\mathrm{d}\tilde{t} = 0. \tag{21}$$

In Eq. (21) the terms within brackets are constant on a limit cycle. Hence, for Eq. (21) to be true, the individual terms within the brackets must be equal, *i.e.*,

$$2\xi \left(\frac{q_1}{\varepsilon_s}\right) \sin(\varphi_1) = \frac{\omega L_0}{\pi \tilde{c}_0} \zeta \qquad (22)$$

Equation (22) describes the balance between driving (LHS) and damping (RHS) processes on a limit cycle. Note that the gain, q_1/ε, and the phase of the velocity-coupled FDF, φ_1, are explicitly related by the damping factor, ζ, on a limit cycle. With the FDF computed in §5, the above equation can be used to find the limit cycle amplitude, ε_s. The stability of limit cycles is obtained by calculating the gradient of the LHS of Eq. (21) with respect to ε, *i.e.*,

$$\left[\frac{\partial}{\partial \varepsilon} \int_{t'}^{t'+T} \left(2\xi q_1 \sin(\varphi_1) - \frac{\omega L_0}{\pi \tilde{c}_0} \zeta \varepsilon\right) \sin^2(\omega \tilde{t}) \mathrm{d}\tilde{t}\right]_{\varepsilon_s} < 0 \qquad (23)$$

implies that the limit cycle is stable.

Figure 11 shows the cyclic integral of rate of change of energy (CIRCE), the LHS of Eq. (21), as a function
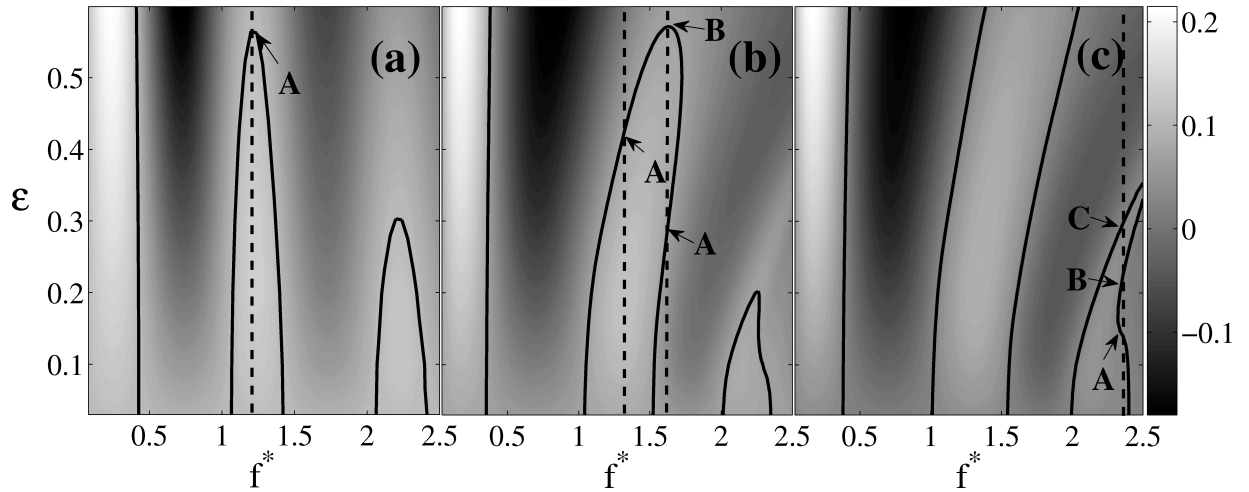

Figure 11: CIRCE diagram showing the net energy change over one cycle of oscillation, LHS of Eq. (21), as a function of velocity perturbation amplitude across thermoacoustic systems with different natural frequencies. (a) $K = 1$, $\zeta = 0.06$; (b) K from DNS, $\zeta = 0.14$; and (c) K from DNS, $\zeta = 0.06$. The grey-scale is such that regions where driving exceeds damping are light, while regions where damping exceeds driving are dark. The black boundaries between light and dark regions are limit cycles. The dashed lines in each frame represent the scenarios examined in Fig. 12.

of velocity perturbation amplitude, ε, across thermoacoustic systems with different natural frequencies, f^*. Here $f^* = \tilde{c}_0 L_f / 2u_0 L_0$ and therefore, for a given flame, variation in f^* corresponds to varying duct lengths, or conversely, for a given duct, variation in f^* corresponds to varying flame height or varying Mach number. This figure shows the effect of the type of velocity model and strength of damping on limit cycle behaviour across a range of thermoacoustic systems. Figure 11(a) corresponds to systems with $K = 1$ and Fig. 11(b) and (c) correspond to systems with the K shown in Fig. 5. The damping factor, ζ, is 0.06, 0.14 and 0.06 for Fig. 11(a), (b) and (c) respectively. As described in §4, $\zeta = 0.06$ for a Rijke tube of length 70 *cm*, diameter 10 *cm* and average duct temperature of 350 *K*. The higher damping value of $\zeta = 0.14$ corresponds to a Rijke

tube of length 50 cm, diameter 12 cm and average temperature 330 K. A lower damping value of $\zeta = 0.03$, as in Fig. 12(c), corresponds to a Rijke tube of length 100 cm, diameter 6 cm and average temperature 440 K. These numbers were chosen because they resemble laboratory-scale experiments. The grey-scale is such that regions where driving exceeds damping are light, while regions where damping exceeds driving are dark. The black boundaries between light and dark regions are limit cycles. Examining the behaviour along the x-axis at the lowest velocity perturbation amplitude, *i.e.* in the linear limit, shows that there exist bands of instability, as expected from linear stability analysis. For a particular system, the nonlinear behaviour is analyzed by examining the variation in CIRCE at a given f^* as a function of velocity perturbation amplitude. The dashed lines in each frame represent the scenarios examined in the Fig. 12, in terms of the number of limit cycles that exist and their stability.
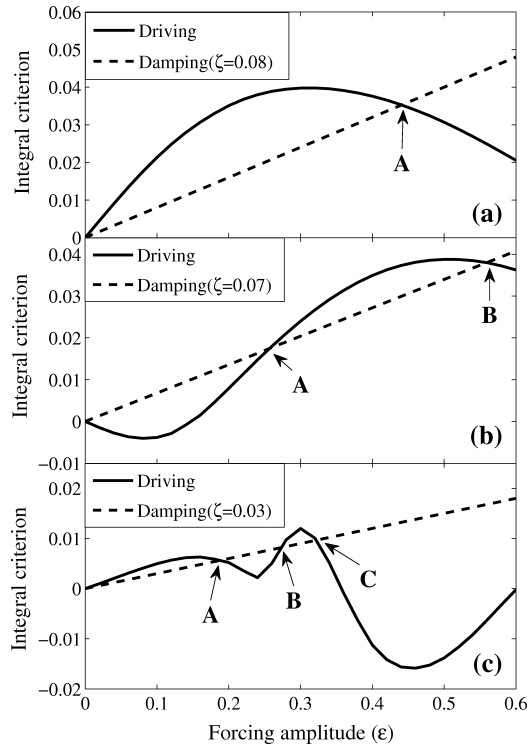

Figure 12: CIRCE for thermoacoustic systems with different fundamental frequencies (duct lengths), (a) Slice of Fig. 11(b) at $f^* = 1.4$, A - stable limit cycle, and (b) Slice of Fig. 11(b) at $f^* = 1.6$, A - unstable limit cycle, B - stable limit cycle (c) Slice of Fig. 11(c) at $f^* = 2.35$, A and C - stable limit cycles, B - unstable limit cycle

In Fig. 12 the solid and dashed lines represent the driving and damping terms of Eq. (21). Figure 12(a) shows a system that is linearly unstable with a stable limit cycle at A, which corresponds to a supercritical bifurcation. On the other hand, Fig. 12(b) shows a system that is linearly stable with an unstable limit cycle at A and a stable limit cycle at B. If the system is given an excitation with amplitude greater than the amplitude of state-A, oscillations in the system will grow until the system reaches state-B. This phenomenon is called triggering [58, 59]. In a single-mode thermoacoustic system, the minimum amplitude of an excitation that can cause triggering is the amplitude at point-A. This corresponds to a subcritical bifurcation. The system shown in Fig. 12(c) is linearly unstable, has stable limit cycles at A and C, and an unstable limit cycle at B. This corresponds to a supercritical bifurcation followed by two fold bifurcations.
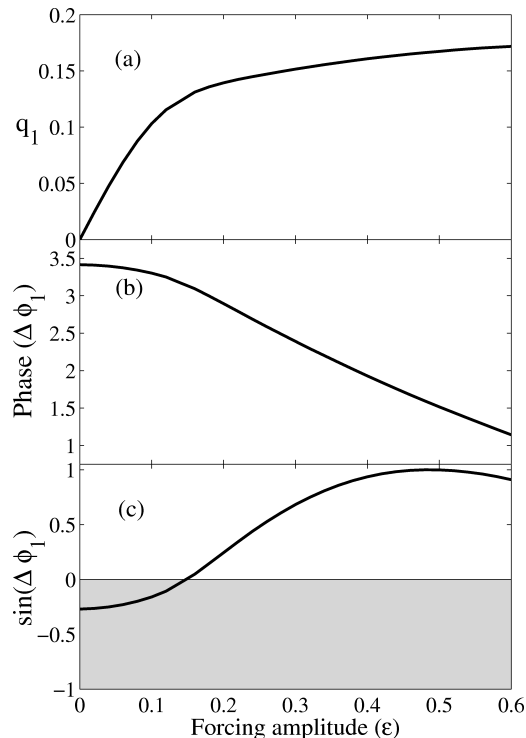
17

Figure 13: Amplitude dependence of the fundamental of heat release rate, q_1, phase, φ_1, and $\sin(\varphi_1)$, at $f^* = 1.6$. The subcritical behaviour of Fig. 12(b) is due to change in sign of $\sin(\phi)$ due to the large variation of the phase.

The variations in the scenarios seen here are due to the amplitude-dependence of the gain and phase of the FDF [35] and their contributions to the driving term in Eq. 22. The supercritical bifurcation seen in Fig. 12(a) arises because the gain decreases as the forcing amplitude increases, while the phase remains fairly constant (see Fig. 9 (a) and (b)). The subcritical bifurcation seen in Fig. 12(b) arises because the phase changes significantly as the amplitude increases, as shown in Fig. 13(b). Crucially, this significant change in phase results in a change in sign of the $\sin(\varphi_1)$ factor in the driving term from negative at low amplitudes (grey patch) to positive at higher amplitudes (white patch) (Fig. 13(c)), which allows the existence of an unstable and a stable limit cycle. Physically, this means that the heat release changes from being stabilizing at small amplitudes to being destabilizing at large amplitudes, which implies that the system is linearly stable but susceptible to triggering and therefore must have a subcritical bifurcation. The supercritical bifurcation followed by two fold bifurcations seen in Fig. 12(c) is because the gain does not decrease monotonically but first decreases, then increases and then decreases again, as the forcing amplitude increases, i.e. it has two inflection points. Over this range of amplitudes, the heat release always remains destabilizing ($\sin(\phi)$ is positive) and therefore three limit cycles exist, one of which is unstable.

Preetham _et al._ in their study of the nonlinear dynamics of premixed flames defined the driving term, $H(\epsilon)$, to be equal to the gain of the FDF [1]. The phase was not included in calculating the driving term (see Fig. 22 in [1]). Based on this definition they concluded that the nature of limit cycles depended solely on the concavity of the FDF gain dependence upon the forcing amplitude. However, Eq. 22 can be satisfied only when $\sin(\phi)$ is positive, i.e. only for certain values of the FDF phase. Therefore both the gain and the phase, and their dependence on the forcing amplitude, determine the number of limit cycles that exist and their

18

stabilities. Under certain conditions either the gain or the phase may dominate. When the phase variation is small and the heat release is destabilizing ($\sin(\phi) > 0$), then the amplitude dependence of the gain is more important. However, if the phase variation is large, then both the gain and phase are important, but the amplitude-dependence of the phase determines whether the heat release is stabilizing or destabilizing and when an abrupt switch from one to the other occurs.

Most importantly, when K is assumed to be unity, only supercritical bifurcations are possible (Fig. 11(a)). This is because a limit cycle is established solely due to the decrease in the gain of the FDF as the amplitude increases (see Fig. 9(c)) and the phase has no role to play because it does not vary with the forcing amplitude (see Fig. 9(d)). Figures 11 (b) and (c), which are seen only in simulations with the realistic velocity field, however, show clearly that when the phase speed is not equal to the mean flow velocity the nonlinear behaviour is more complex and different types of bifurcation are possible due to large variations in the gain and phase of the FDF.

7. Conclusions

This paper examines the influence of the perturbation velocity field on the nonlinear thermoacoustic behaviour of a simple premixed flame in a tube. A reduced order model of the perturbation velocity field is obtained from forced Direct Numerical Simulation (DNS) of a 2-D premixed flame. The DNS show that the perturbation velocity can be simplified to a travelling wave with a frequency-dependent phase speed. The most important difference between this reduced order model and velocity models used currently is that the phase speed is not assumed to be equal to the mean streamwise flow velocity.

For thermoacoustic calculations, the flame is modelled using a nonlinear kinematic model based on the G-equation with the velocity model obtained from the DNS, while the acoustics are governed by linearised momentum and energy equations. Using open-loop forced simulations, the flame describing function (FDF) is calculated. The FDF phase has a strong amplitude-dependence, unlike that of past analyses which assumed the phase speed of velocity pertubations to be equal to the mean streamwise flow velocity.

Assuming the existence of limit cycles, integral criteria are derived for a single mode thermoacoustic system in order to calculate the amplitudes of limit cycles and their stability. The existence and stability of these limit cycles is then explained using the amplitude-dependence of the gain and phase of the FDF. When the phase speed of velocity perturbations is assumed to equal the mean streamwise flow velocity, the system can have only one stable state. For the velocity model derived from DNS results, however, several limit cycles exist and the system has combinations of fold bifurcations and either supercritical or subcritical Hopf bifurcations, depending on the operating condition. We find that these multiple limit cycles are caused by the large variation in the gain and phase of the FDF as the oscillation amplitude increases. This variation arises because the velocity perturbations are not convected exactly at the mean streamwise flow velocity. This shows that the phase speed of velocity perturbations has a strong influence on the nonlinear thermoacoustic behaviour of ducted premixed flames.

8. Acknowledgments

References

[1] Preetham, S. Hemchandra, T. C. Lieuwen, J. Propul. Power 394 (2008) 51–72.

[2] S. H. Preetham, T. C. Lieuwen, Proc. Combust. Inst. 31 (2007) 1427–1434.

[3] S. Hemchandra, N. Peters, T. Lieuwen, Proc. Combust. Inst. 33 (2011) 1609–1617.

[4] A. P. Dowling, J. Fluid Mech. 394 (1999) 51–72.

[5] S. Ducruix, D. Durox, S. Candel, Proc. Combust. Inst. 28 (2000) 765–773.

[6] D.-H. Shin, D. V. Plaks, T. Lieuwen, U. M. Mondragon, C. T. Brown, V. G. McDonell, J. Propul. Power 27 (2011) 105–116.

[7] P. Subramanian, R. I. Sujith, J. Fluid Mech. 679 (2011) 315–342.

[8] O. Graham, A. Dowling, in: ASME Turbo Expo ASME GT2011-45255, 2011.

[9] B.-T. Chu, L. S. G. Kovasznay, J. Fluid Mech. 3 (1958) 494–514.

[10] J. Wu, A. Vakili, J. Wu, Progress in Aerospace Sciences 28 (1991) 73 – 131.

[11] K. McManus, U. Vandsburger, C. Bowman, Combust. Flame 82 (1990) 75–92.

[12] J. U. Schluter, Large-eddy simulations of combustion instability by static turbulence control, Technical Report, Center for Turbulence Research Annual Research Briefs, 2001.

[13] D. Wee, S. Park, T. Yi, A. Annaswamy, A. Ghoniem, in: 40th AIAA Aerospace Sciences Meeting and Exhibit.

[14] L. Boyer, J. Quinard, Combust. Flame 82 (1990) 51 – 65.

[15] F. Baillot, D. Durox, R. Prud'homme, Combust. Flame 88 (1992) 149 – 168.

[16] D. H. Ferguson, D.-H. Lee, T. Lieuwen, G. A. Richards, in: Proceedings of the 2005 Joint States Meeting of the Combustion Institute.

[17] A. Birbaud, D. Durox, S. Candel, Combust. Flame 146 (2006) 541 – 552.

[18] A. L. Birbaud, D. Durox, S. Ducruix, S. Candel, Physics of Fluids 19 (2007) 013602.

[19] D. Durox, T. Schuller, S. Candel, Proc. Combust. Inst. 30 (2005) 1717–1724.

[20] D. Durox, T. Schuller, N. Noiray, S. Candel, Proc. Combust. Inst. 32 (2009) 1391 – 1398.

[21] V. Kornilov, K. Schreel, L. de Goey, Proc. Combust. Inst. 31 (2007) 1239 – 1246.

[22] V. Kornilov, R. Rook, J. ten Thije Boonkkamp, L. de Goey, Combustion and Flame 156 (2009) 1957–1970.

[23] N. Karimi, M. J. Brear, S.-H. Jin, J. P. Monty, Combust. Flame 156 (2009) 2201 – 2212.

[24] S. Kartheekeyan, S. R. Chakravarthy, Combust. Flame 146 (2006) 513–529.

[25] S. J. Shanbhogue, T. C. Lieuwen, in: ASME Turbo Expo GT2006-90302, 2006.

[26] S. Shanbhogue, D.-H. Shin, S. Hemchandra, D. Plaks, T. Lieuwen, Proc. Combust. Inst. 32 (2009) 1787–1794.

[27] J. O'Connor, T. Lieuwen, J. Eng. Gas Turbines Power 134 (2012).

[28] J. O'Connor, T. Lieuwen, Combust. Sci. Technol. 183 (2011) 427–443.

[29] J. O'Connor, T. Lieuwen, Physics of Fluids 24 (2012) 075107–075107–30.

[30] T. Schuller, S. Ducruix, D. Durox, S. Candel, Proc. Combust. Inst. 29 (2002) 107–113.

[31] T. Schuller, D. Durox, S. Candel, Combust. Flame 134 (2003) 21 – 34.

[32] A. Cuquel, D. Durox, T. Schuller, in: 7th Mediterranean Combustion Symposium, 2011.

[33] K. Kashinath, S. Hemchandra, M. P. Juniper, in: ASME Turbo Expo ASME GT2012-68726, 2012.

[34] N. Noiray, D. Durox, T. Schuller, S. Candel, J. Fluid Mech. 615 (2008) 139–167.

[35] F. Boudy, D. Durox, T. Schuller, S. Candel, Proc. Combust. Inst. 33 (2011) 1121 – 1128.

[36] L. Kabiraj, R. I. Sujith, in: ASME Turbo Expo GT2011-46155, 2011.

[37] C. A. Kennedy, M. H. Carpenter, Appl. Numer. Math. 14 (1994) 397–433.

[38] S. Hemchandra, Combust. Flame 159 (2012) 3530–3543.

[39] G. Lacaze, E. Richardson, T. Poinsot, Combust. Flame 156 (2009) 1993–2009.

[40] B. J. McBride, S. Gordon, M. A. Reno, Coefficients for Calculating Thermodynamic and Transport Properties of Individual Species, Technical Report, NASA TM 4513, 1993.

[41] C. R. Wilke, Chem. Phys. 18 (1950) 517–519.

[42] S. Mathur, P. K. Tondon, S. C. Saxena, Mol. Phys. 12 (1967) 569.

[43] Shreekrishna, S. Hemchandra, T. Lieuwen, Combust. Theor. Modell. 14 (2010) 681–714.

[44] L. Kabiraj, R. I. Sujith, J. Fluid Mech. 713 (2012) 376–397.

[45] F. A. Williams, Turbulent Combustion in The Mathematics of Combustion (ed J. D. Buckmaster), Society for Industrial and Applied Mathematics, 1985, 97–131.

[46] T. Lieuwen, Proc. Combust. Inst. 30 (2005) 1725 – 1732.

[47] G. S. Jiang, D. Peng, SIAM J. Sci. Comp. 21 (2000) 2126–2143.

[48] S. Gottlieb, C. Shu, Math. Comput. 67 (1998) 73–86.

[49] D. Peng, J. Comput. Phys. 155 (1999) 410–438.

[50] P. Smereka, J. Comput. Phys. 211 (2006) 77–90.

[51] A. P. Dowling, J. Fluid Mech. 346 (1997) 271–290.

[52] Preetham, S. K. Thumuluru, H. Santosh, T. Lieuwen, J. Propul. Power 26 (2007) 524–532.

[53] I. Matveev, Thermo-acoustic instabilities in the Rijke tube: Experiments and modeling, Ph.D. thesis, California Institute of Technology, 2003.

[54] M. P. Juniper, J. Fluid Mech. 667 (2011) 272–308.

[55] D. Durox, F. Baillot, G. Searby, L. Boyer, J. Fluid Mech. 350 (1997) 295–310.

[56] V. N. Kornilov, Experimental research of acoustically perturbed bunsen flames, Ph.D. thesis, Eindhoven University of Technology, 2006.

[57] F. E. C. Culick, Acta Astro. 3 (1976) 715 – 734.

[58] F. E. C. Culick, V. Burnley, G. Swenson, J. Propul. Power 11 (1995) 657–665.

[59] J. M. Wicker, W. D. Greene, S. Kim, V. Yang, J. Propul. Power 12 (1996) 1148–1156.